# Scattering of fast electrons by lattice vibrations

Tore Niermann*

*Technische Universität Berlin, Institut für Optik und Atomare Physik, Straße des 17. Juni 135, 10823 Berlin, Germany*

(Received 22 May 2019; revised manuscript received 16 September 2019; published 8 October 2019)

Several aspects of phonon scattering in the transmission electron microscope are investigated with focus on the physically distinct effects of the thermal average over initial states as well as the excitation or annihilation of phonons. Coupled-channel calculations for the model system of a single atom in a harmonic potential are presented and interpreted in terms of inelastic scattering and thermal fluctuations. Furthermore, common approximations for inelastic scattering calculations are compared to this model. Additionally, the description of phonon scattering by means of an *S*-matrix approach is investigated. The *S*-matrix approach allows differentiation between scattering events and propagation of scattered waves within the specimen. Within this approach, it is rigorously proven that by suitable integration over calculations with static atomic coordinates inelastic phonon scattering can be approximated for any initial object state. The limits of this approximation are discussed.

DOI: 10.1103/PhysRevB.100.144305

## I. INTRODUCTION

Atomic resolution in scanning transmission electron microscopy (STEM) is currently most widely achieved by means of high-angle annular dark field (HAADF) imaging. HAADF detectors collect those electrons, which have been scattered into large angles, typically above 50 mrad, with primary electron energies in the range of a few 100 keV. These electrons are known to exhibit a strong dependence on the atomic number of the scatterer, while being rather insensitive to dynamic scattering effects, as often found for smaller angles in crystalline specimens [1]. The largest part of the scattered signal at higher angles is connected to electron-phonon scattering [2].

Two physically distinct effects must be considered, when electron-phonon scattering within a transmission electron microscope (TEM) is discussed [3]: inelastic scattering, which is the generation or annihilation of one or more phonons by the fast electrons, and the mixed initial state of the object due to thermal fluctuations. The latter causes the measurements (the diffraction pattern, the high-resolution image, etc.) to become incoherently averaged over several quantum mechanical initial object states during the time of the exposure. In general, both effects act in parallel.

In principle, experiments can be devised to separate the effects; however, these experiments are hard to be realized in practice: For instance, state filtering can be achieved by off-axis electron holography with reference areas far away from the specimen [4,5], or measurements can be performed at absolute zero temperature, where the object is initially in its ground state, which is pure.

For extended specimens, i.e., more than a single atom, a further effect must be considered for electron scattering: the effect of multiple scattering (elastic as well as inelastic) within the specimen. Theoretically, single scattering corresponds to the description of the interaction between the fast electron and the specimen within the first-order Born approximation, while the description of multiple scattering contains higher order terms of the Born series. Multiple scattering and the fact that the measured intensity is quadratic in the wave function results in a nonlinear relationship between the interaction potential itself and the eventually measured quantity.

For a fast electron multiple scattering at a specimen consisting of many local scattering centers like atoms can discussed in two extremes: One extreme treats the object with all its atoms and internal states as a single nonlocal entity and the fast electron is scattered multiple times at this extended target, and the other extreme treats the atoms in the object as independent targets and the electron is scattered locally at most a single time at the individual atoms. This fast electron might be scattered by many different atoms on its path through the specimen.

For the vibrational subsystem of the specimen, the above extreme of independent scattering centers corresponds to a model, where each atom has its own quantum mechanical vibration state, and these vibrations are independent of the vibrations of the other atoms, as, for instance, assumed in the Einstein model. However, the approach of treating the specimen as individually vibrating atoms comes to its limits, when phonon scattering is considered. Phonons correspond to correlated vibrations, and multiple neighboring atoms swing collectively. Since the movement of the neighboring atoms influences each atom, the object cannot be treated as a collection of individual scattering centers. The whole object must be treated as an extended multiatomic scatterer and the fast electron is scattered multiple times at this nonlocal scatterer.

Nevertheless, there are cases even for the extended specimen where single scattering is a sufficient description of the underlying physics and multiple scattering effects can be neglected. This is, for instance, the case in very thin specimens consisting of light elements. This is also the case for x-ray

*tore.niermann@tu-berlin.de

 

scattering, where the interaction itself is very weak compared to electron scattering. For this reason, the first descriptions in literature about the effects of phonons can be found for x-ray scattering within the first-order Born approximation. Most of the discussions can be extended to the electron scattering case.

The first-order Born approximation and the assumption of independently vibrating atoms allow to simply model the effect of the thermal average: The scattered electron exit wave is given by the exit wave obtained for the thermally averaged object. This is basically what is usually done by including the Debye-Waller factor into the calculation. In a crystalline specimen, the thermal averaged potential is also periodic. Since a wave scattered from a periodic specimen is only scattered into discrete angles, the calculated diffraction patterns resulting from the use of the Debye-Waller factor only exhibit intensity in the Bragg reflections.

However, even in the single scattering case, a diffuse background between the Bragg reflections can be found in diffraction patterns. Within the x-ray scattering literature this background is referred to as thermal diffuse scattering (TDS). Within the single scattering approximation, this diffuse background occurs due to the quadratic nature of the registered intensity. The terms describing this background are not correctly reproduced by the use of the Debye-Waller factor. However, for crystalline specimens, these terms are usually small and often neglected: For a specimen consisting of $N$ scattering centers, only $N$ of a total of $N^2$ terms are described incorrectly [6–8].

These TDS terms can also be further investigated within the limits of the first-order Born approximation for correlated vibrations [9]. As discussed above, for electron scattering often the first-order Born approximation does not hold and multiple scattering effects must be considered [10]. Inelastic phonon scattering also contributes to the diffuse background found between Bragg peaks [11]. Also, the intensity of the Bragg reflections is found to be incorrectly described by the Debye-Waller factor in the multiple scattering case [3].

Earlier publications concerned with electron-phonon scattering often concentrated on the definition of absorption coefficients for a wave, which is elastically scattered at the thermally averaged potential [12,13]. Alternative approaches for the calculation of absorption coefficients using a single inelastic scattering approximation can also be found in the literature for individually vibrating atoms as well as for correlated vibrations [14,15].

Further experimental insight into electron-phonon scattering can in principle be achieved by electron energy loss spectroscopy (EELS). Since the energy losses (gains) for single-phonon creation (annihilation) are in the range of a few milli electron volts, this requires spectrometers with high energy resolution. Since such spectrometers have become commercially available [16], a deeper understanding of the underlying physics becomes necessary. Recent phonon spectroscopy experiments confirm that electrons scattered into typical HAADF angles carry energy losses which can be attributed to phonon excitations [17].

For the calculation of inelastic scattering cross sections for the interpretation of EELS experiments, commonly approximations are required to reduce the calculation efforts. The validity of these approximations are seldom investigated or even discussed. A correct calculation of the phonon cross sections should thermally average the inelastic cross sections over initial states, which is an average of terms at least quadratic in the potential. A common approximation is to calculate the inelastic cross section of a thermally averaged potential or include thermally averaged occupation numbers in this cross section, which instead results in quadratic (and higher order) terms of an averaged potential [11,18–20].

For a quantitative evaluation of HAADF images, even minute details of the electron scattering must be considered, and thus the need for image calculations arises. For these calculations of HAADF images, usually the observables (e.g., the diffraction pattern) obtained from conventional simulations for a set of given static atom positions (e.g., by the multislice method) are averaged over different atomic positions [21,22]. The atomic positions in turn are sampled from the probability density of the phonon model. Within this respect, this approach is a Monte Carlo integration over the atom positions' probability of the measured observable [23]. This approach is not limited to independently vibrating atoms and can also applied for correlated atomic motions [3,24,25].

Empirically it is found that this approach matches experimental observations of high-angle diffraction patterns, thus also HAADF images, very well [24,26]. The justification of this approach is often done on the basis of the semiclassic argument that the motion of the atoms is so slow compared to the fast electron that the electron sees frozen atomic configurations. This justification is called the frozen phonon (FP) approximation (also called the frozen lattice approximation). Previous studies can be found in the literature, where the validity of this approach is proven for cases of single inelastic scattering and independently vibrating atoms, i.e., where only single scattering at independent targets is assumed [27–31]. Other studies prove equivalence of this approach with the results obtained for a thermally averaged object state [31,32]. However, at temperatures $T > 0$ K, a system in thermal equilibrium with its environment cannot be described by a pure state anymore [33], and thus the physical meaning of this thermally averaged object state is unclear. This must be considered in the description of electron-phonon scattering, as already was mentioned in Ref. [28].

The quantum excitations of phonons (QEP) model [23,34] allows calculation of partial wave functions for electrons corresponding to a given final phonon state of the object for the case in which the object was initially in a phonon eigenstate. By inelastically averaging over final states and atom coordinates, the final electron probability can be obtained. When the thermal average over initial object states is calculated, the same result as in the frozen phonon approximation is obtained.

In this work, various aspects of electron-phonon scattering are investigated in detail. Numerical calculations using the coupled channels approach of Yoshioka [14] are presented, which show the influences of inelastic phonon scattering in comparison to thermal averaging. In the numerical calculations, a simple model system for electron-phonon scattering is utilized: the scattering of the fast electron at a single atom, which is placed in a harmonic potential. This model resembles an atom within a crystal, which is forced into its equilibrium position due to the interaction with its neighboring atoms. This also corresponds to a single atom

within an extended specimen, when it is assumed that each atom vibrates on its own in the crystal potential created from its neighbors. Obviously, this model will not reproduce effects of correlated vibration or other typical diffraction effects of extended crystals, like Kikuchi bands, nor will this model give realistic energy loss spectra, since it exhibits a nonrealistic dispersion relation. Nevertheless, the fundamental properties of the electron-phonon scattering as well as the influences due to the ensemble of initial object states can be studied by such a model. A discussion about the differences resulting from the use of an Einstein model in comparison to a full phonon model can be found in the work of Forbes *et al.* [20].

The numerical calculations are performed without further approximations of the interaction potential itself. This allows to study also the validity of common approximations for the calculation of inelastic scattering cross sections within this model.

Furthermore, it is investigated how conventional calculations like the multislice method can be used to calculate aspects of electron-phonon scattering. This investigation is carried out within the general quantum mechanical scattering matrix ($S$-matrix) approach [10,35]. The joint wave function of object and fast electron is expanded in a Born series in a plane-wave base for the electron. The comparison of the $S$ matrix of the full scattering description with an $S$-matrix description of a conventional scattering simulation with static atomic coordinates reveals that electron-phonon scattering can be sufficiently accurately described by such simulations with static atomic positions. Phonon-related cross sections can be calculated by integrating the results of these simulations over phonon states. We refer to this approximation by means of integrals over conventional simulations as static approximation.

For single scattering, i.e., the first-order term of Born series, the static approximation is exact. For multiple scattering, a further requirement regarding the extents of the specimen is needed, which assures the dephasing of partial waves belonging to different object states in between scattering events can be neglected. This requirement is usually sufficiently well fulfilled for phonon scattering at medium energies ($>100$ keV).

As a corollary of this static approximation, the calculation result obtained by averaging conventional simulations over atomic configurations, as done in the frozen phonon method, describes the underlying electron-phonon scattering and thermal averaging correctly. The only additional requirement for correctness for this static approximation the frozen phonon method is the correct registration of all scattered electrons regardless of their energy loss.

In contrast to the works of Wang [32] and van Dyck [31], the intermediate step of an averaged potential is avoided, and thus no assumption of individually vibrating atoms or equivalence of elastic and average interaction terms must be required. Also, no incoherence between intermediate inelastic states must be externally superimposed. The $S$-matrix description already includes all coherency effects. The resulting equations for key quantities within this static approximation are formally similar to equations obtained within the QEP model [23]. The presented proof shows that the equations for inelastic cross sections found for the QEP model can also be applied for arbitrary initial object states, not only eigenstates. Furthermore, the validity of the approximation can be related to the object size.

In Sec. II, the relevant physical quantities and the used notation are introduced. Section III introduces the static approximation and proves the equivalence between a full quantum mechanical treatment of electron-phonon scattering and the calculation performed in frozen phonon simulations. Section IV describes the underlying equations and methods used in the numerical evaluation. The results of this evaluations are presented in Sec. V.

## II. THEORY

### A. Basics

The whole system consists of two parts, the fast electron itself and the object, which scatters the electron. In general, the object will consists of many particles, nuclei, and electrons. For the investigation of phonon scattering, the electronic excitations of the object are ignored and it is assumed that the object's electrons follow adiabatically the position of the nuclei. The vector $\boldsymbol{R} = (\boldsymbol{R}_1, \boldsymbol{R}_2, \dots)$ represents a high-dimensional vector describing the coordinates $\boldsymbol{R}_1, \boldsymbol{R}_2, \dots$ of all the object's atoms. The dynamics of the atom positions still depend on the internal electronic excitations of the object; however, these details are not important for the discussion in this paper and are hidden in an object internal Hamiltonian $\widehat{H}_{\text{obj}}(\boldsymbol{R})$. We assume the corresponding object eigenfunctions are known,

$$\widehat{H}_{\text{obj}} |n\rangle = \mathcal{E}_n |n\rangle ,$$

and form a complete and orthonormal set. The index $n$ represents all internal quantum numbers of the object.

The Hamiltonian of the full system in coordinate representation is

$$\widehat{H}(\boldsymbol{r}, \boldsymbol{R}) = \frac{\hbar^2}{2m_0} \Delta_r + \widehat{H}_{\text{obj}}(\boldsymbol{R}) + \widehat{V}(\boldsymbol{r}, \boldsymbol{R}), \tag{1}$$

where $\boldsymbol{r}$ is the fast electron's position and $\Delta_r$ is the Laplace operator with respect to this coordinates.

The operator $\widehat{V}$ describes the Coulomb interaction between the fast electron and the object's particles. $m_0$ is the electron's rest mass. The interaction $\widehat{V}$ is diagonal in position space:

$$\langle \boldsymbol{r}, \boldsymbol{R} | \widehat{V} | \boldsymbol{r}', \boldsymbol{R}' \rangle = V(\boldsymbol{r}, \boldsymbol{R}) \langle \boldsymbol{r} | \boldsymbol{r}' \rangle \langle \boldsymbol{R} | \boldsymbol{R}' \rangle . \tag{2}$$

Far away from the scattering center, i.e., where the interaction potential between object and electron $\widehat{V}$ is negligible, the Hamiltonian becomes the Hamiltonian of the two free (noninteracting) systems:

$$\widehat{H}_0(\boldsymbol{r}, \boldsymbol{R}) = \frac{\hbar^2}{2m_0} \Delta_r + \widehat{H}_{\text{obj}}(\boldsymbol{R}). \tag{3}$$

The eigenstates of this Hamiltonian are given by the products of the object eigenstates $|n\rangle$ and the eigenstates of the free electron, i.e., plane waves characterized by their wave vector $\boldsymbol{k}$, and form a complete set:

$$\langle \boldsymbol{r} | \boldsymbol{k}, n \rangle = \exp(\mathrm{i} 2\pi \boldsymbol{k} \cdot \boldsymbol{r}) |n\rangle .$$

The total energy $E$ of the full system of electron and object is conserved. For a given total energy $E$ and an object in state

$n$, the corresponding wave number $k$ is given by the relativistic dispersion relation

$$E - \mathcal{E}_n + m_0c^2 = m_0c^2\sqrt{1 + \frac{h^2k^2}{m_0^2c^2}}, \tag{4}$$

where $c$ the vacuum light speed. For the two noninteracting systems, the total energy is given by the sum of the object's energy and the electron's energy $eU_{\mathrm{acc}}$, which is determined by the acceleration voltage $U_{\mathrm{acc}}$ and $e$ the elementary charge.

Through the interaction, an energy $\Delta E$ may be transferred from the electron to the object or vice versa. Since the relevant excitation energies for phonon scattering are typically small (few meV) compared to the electron's energy (few hundred keV), the wave number after an electron energy loss ($\Delta E > 0$) or gain ($\Delta E < 0$) can be approximated by

$$k(\Delta E) = K - \frac{\sigma}{2\pi e}\Delta E + \mathcal{O}(\Delta E^2), \tag{5}$$

with the initial electron's wave number $K$

$$\frac{(hK)^2}{2m_0} = eU_{\mathrm{acc}}\left[1 + \frac{eU_{\mathrm{acc}}}{2m_0c^2}\right]$$

and

$$\sigma = \frac{1}{K}\frac{2\pi m_0 e}{h^2}\left[1 + \frac{eU_{\mathrm{acc}}}{m_0c^2}\right].$$

The scattering matrix ($S$-matrix) element

$$\langle \boldsymbol{k}_{\mathrm{f}}, n_{\mathrm{f}}|\widehat{S}|\boldsymbol{k}_{\mathrm{i}}, n_{\mathrm{i}}\rangle$$

describes the complex scattering amplitude from an initial state, which at times $t \to -\infty$ corresponds to an asymptotic state $|\boldsymbol{k}_{\mathrm{i}}, n_{\mathrm{i}}\rangle$, into a final state, which corresponds at times $t \to +\infty$ to an asymptotic state $|\boldsymbol{k}_{\mathrm{f}}, n_{\mathrm{f}}\rangle$. Appendix A describes how the elements of the $S$ matrix can be calculated in general.

### B. Initial density matrix

Typically the fast electron and the object are initially not in a pure state but in a mixed state. Let $\widehat{\rho}_{\mathrm{i}}^{(\mathrm{el})}$ be the density operator for the initial state of the fast electron. The object is initially in a thermal average, and thus its density operator is diagonal in the spectral basis:

$$\widehat{\rho}_{\mathrm{i}}^{(\mathrm{obj})} = \sum_n p_n\,|n\rangle\,\langle n| \tag{6}$$

with a suitable distribution function $p_n$, e.g., the Boltzmann distribution

$$p_n = \frac{\exp(-\beta\mathcal{E}_n)}{\sum_n g_n \exp(-\beta\mathcal{E}_n)}$$

with $\beta = 1/k_BT$ and the degeneration factor $g_n$. The probability to find an object at a given coordinate $\boldsymbol{R}$ is

$$p(\boldsymbol{R}) = \langle \boldsymbol{R}|\widehat{\rho}_{\mathrm{i}}^{(\mathrm{obj})}|\boldsymbol{R}\rangle = \sum_n p_n\,\langle \boldsymbol{R}|n\rangle\,\langle n|\boldsymbol{R}\rangle\,, \tag{7}$$

and it must be stressed here that in general

$$\widehat{\rho}_{\mathrm{i}}^{(\mathrm{obj})} \neq \int dR\, p(\boldsymbol{R})\,|\boldsymbol{R}\rangle\,\langle \boldsymbol{R}|\,;$$

i.e., the initial density matrix of the object is not diagonal in objects coordinates. Here and in the following, we use the notation $dR \equiv dR_1^3 dR_2^3 \ldots$.

The density matrix of the initial state is then given by the tensor product

$$\widehat{\rho}_{\mathrm{i}} \equiv \widehat{\rho}_{\mathrm{i}}^{(\mathrm{el})} \otimes \widehat{\rho}_{\mathrm{i}}^{(\mathrm{obj})}. \tag{8}$$

### C. Final density matrix

The $S$-matrix formulation can be used to formally calculate the density matrix of the final states, from the initial density matrix $\widehat{\rho}_{\mathrm{i}}$:

$$\widehat{\rho}_{\mathrm{f}} = \widehat{S}\widehat{\rho}_{\mathrm{i}}\widehat{S}^{\dagger},$$

where the dagger denotes the adjoint operator.

We introduce here three variants of density operators $\widehat{\rho}_{\mathrm{f}}^{(\mathrm{el})}$, which can be used to calculate various measurements of the final state of the fast electron. Furthermore, we assume a perfect paraxial optical system, which does not exhibit any aberrations. This means that the trajectory of the electron in a classical sense is only dependent on the lateral position and lateral scattering vector in a plane at a given $z$ coordinate. The detector itself will measure the current through the detector plane. This current in turn is proportional to the $z$ component of the electron's wave vector. For electron-phonon scattering, the energy losses and hence the changes in wave number of the fast electron are so minute that this factor is assumed constant in the following.

When all final electrons independent of the energy loss (and thus independent of the final state of the object) are measured, the density operator of the fast electron is given as the subtrace over all object states:

$$\begin{aligned}\widehat{\rho}_{\mathrm{f}}^{(\mathrm{el,total})} &= \mathrm{Tr}_{\mathrm{obj}}[\widehat{\rho}_{\mathrm{f}}] = \sum_n \langle n|\widehat{\rho}_{\mathrm{f}}|n\rangle \\ &= \sum_{n,n'} p_{n'}\,\langle n|\widehat{S}|n'\rangle\,\widehat{\rho}_{\mathrm{i}}^{(\mathrm{el})}\,\langle n'|\widehat{S}^{\dagger}|n\rangle\,.\end{aligned} \tag{9}$$

In the following, quantities deferred from $\widehat{\rho}_{\mathrm{f}}^{(\mathrm{el,total})}$ are referred to as "total" quantities (e.g., total cross section), since they consider all final electrons regardless of the object state.

When an idealized energy filter is applied, which only lets electrons pass which have undergone a certain energy loss $\Delta E$, the resulting density operator of the fast electron is

$$\widehat{\rho}_{\mathrm{f}}^{(\mathrm{el,filtered})}(\Delta E) = \sum_{n,n'|\mathcal{E}_n = \mathcal{E}_{n'} + \Delta E} p_{n'}\,\langle n|\widehat{S}|n'\rangle\,\widehat{\rho}_{\mathrm{i}}^{(\mathrm{el})}\,\langle n'|\widehat{S}^{\dagger}|n\rangle\,. \tag{10}$$

From this density matrix, we can also derive "elastic" and "inelastic" density matrices, with the latter referring to electrons which underwent an energy loss and the former referring to those which did not:

$$\begin{aligned}\widehat{\rho}_{\mathrm{f}}^{(\mathrm{el,elastic})} &= \widehat{\rho}_{\mathrm{f}}^{(\mathrm{el,filtered})}(0), \\ \widehat{\rho}_{\mathrm{f}}^{(\mathrm{el,inelastic})} &= \widehat{\rho}_{\mathrm{f}}^{(\mathrm{el,total})} - \widehat{\rho}_{\mathrm{f}}^{(\mathrm{el,elastic})}.\end{aligned} \tag{11}$$

The elastically (using the above definition) scattered electrons may still have changed the object state, e.g., by simultaneously creating and annihilating a phonon of same energy, but with a different wave vector.

In electron holography, the reference wave, as long as it passes far from the object, is entangled with the initial object state. Hence, there will be no interference between partial waves belonging to different object states (even when the electrons energy is still conserved). Such holographic measurements can be described by the (for lack of a better word) "coherent" density matrix:

$$\widehat{\rho}_{\mathrm{f}}^{(\mathrm{el,coherent})} = \sum_n p_n \langle n|\widehat{S}|n\rangle \, \widehat{\rho}_{\mathrm{i}}^{(\mathrm{el})} \, \langle n|\widehat{S}^{\dagger}|n\rangle \,,$$
$$\widehat{\rho}_{\mathrm{f}}^{(\mathrm{el,incoherent})} = \widehat{\rho}_{\mathrm{f}}^{(\mathrm{el,total})} - \widehat{\rho}_{\mathrm{f}}^{(\mathrm{el,coherent})}. \tag{12}$$

### D. Static *S* matrix

The result of scattering can be calculated for fixed atom coordinates using common simulation approaches. We will refer to this scattering at fixed atom as "static" scattering and index the corresponding symbols with "S."

The Hamiltonian corresponding to the static scattering case is only acting on the fast electron and has a parametric dependency on the object coordinates $\boldsymbol{R}$:

$$\widehat{H}_{\mathrm{S}}(\boldsymbol{r};\boldsymbol{R}) = \frac{\hbar^2}{2m_0}\Delta_r + \widehat{V}_{\mathrm{S}}(\boldsymbol{R}), \tag{13}$$

where the interaction operator $\widehat{V}_{\mathrm{S}}(\boldsymbol{R})$ for the static case can be written in terms of the interaction operator $\widehat{V}$ of the full treatment as

$$\langle \boldsymbol{r}|\widehat{V}_{\mathrm{S}}(\boldsymbol{R})|\boldsymbol{r}'\rangle = \langle \boldsymbol{r},\boldsymbol{R}|\widehat{V}|\boldsymbol{r}',\boldsymbol{R}\rangle = V(\boldsymbol{r},\boldsymbol{R})\,\langle \boldsymbol{r}|\boldsymbol{r}'\rangle \,. \tag{14}$$

Also, $S$-matrix elements $\langle \boldsymbol{k}|\widehat{S}_{\mathrm{S}}(\boldsymbol{R})|\boldsymbol{k}'\rangle$ can be defined (see Appendix B), which describes the complex scattering amplitude from an initial asymptotic state $|\boldsymbol{k}'\rangle$ into a final state $|\boldsymbol{k}\rangle$. As mentioned above, for numerical evaluation of $\langle \boldsymbol{k}|\widehat{S}_{\mathrm{S}}(\boldsymbol{R})|\boldsymbol{k}'\rangle$, the common TEM calculation methods like multislice calculations can be used.

## III. STATIC *S*-MATRIX APPROXIMATION AND FROZEN PHONON METHOD

The static $S$-matrix approximation is

$$\langle \boldsymbol{k},\boldsymbol{R}|\widehat{S}|\boldsymbol{k}',\boldsymbol{R}'\rangle \approx \langle \boldsymbol{k}|\widehat{S}_{\mathrm{S}}(\boldsymbol{R})|\boldsymbol{k}'\rangle\,\langle \boldsymbol{R}|\boldsymbol{R}'\rangle \,. \tag{15}$$

Hence, the exact $S$ matrix of the full problem can be approximated by the static $S$ matrix and is approximately diagonal in object coordinates. A rigorous quantum mechanical proof for the approximation (15) is given in Appendix C. This approximation is valid up to $N$th scattering order for a given specimen of size $A$ as long as $2\Delta k\, A \ll 1/(N-1)$ holds for the change of the wave vector $\Delta k$ due to a change in electron energy. For single scattering, (15) is always valid.

Using the approximation (15), the scattering matrix in spectral representation is given by

$$\langle n|\widehat{S}|n'\rangle \approx \int dR\ \langle n|\boldsymbol{R}\rangle\,\widehat{S}_{\mathrm{S}}(\boldsymbol{R})\,\langle \boldsymbol{R}|n'\rangle \,. \tag{16}$$

The scattering matrix elements of (16) can be numerically evaluated by performing TEM calculations for fixed coordinates and calculating an average weighted by $\langle n|\boldsymbol{R}\rangle\,\langle \boldsymbol{R}|n'\rangle$, e.g., by Monte Carlo integration.

A similar equation like (16) was derived by Forbes *et al.* [23] for the scattered electron's partial wave in the QEP model. However, within the QEP model of Forbes *et al.*, the TEM calculations for fixed coordinates (the operators $\widehat{S}_{\mathrm{S}}(\boldsymbol{R})$ in the above notation) will also depend on the initial state $|n'\rangle$, while in the static $S$-matrix approximation (16) these calculations can be performed independently of the initial state.

Inserting the spectral representation (16) into (9) results in a total final electron density matrix of

$$\begin{aligned}
\widehat{\rho}_{\mathrm{f}}^{(\mathrm{el,total})} &= \sum_{n,n'} p_{n'}\,\langle n|\widehat{S}|n'\rangle\,\widehat{\rho}_{\mathrm{i}}^{(\mathrm{el})}\,\langle n'|\widehat{S}^{\dagger}|n\rangle \\
&= \sum_{n,n'} p_{n'}\left[\int dR\,\langle n|\boldsymbol{R}\rangle\,\widehat{S}_{\mathrm{S}}(\boldsymbol{R})\,\langle \boldsymbol{R}|n'\rangle\right] \\
&\quad \times \widehat{\rho}_{\mathrm{i}}^{(\mathrm{el})}\left[\int dR'\,\langle n'|\boldsymbol{R}'\rangle\,\widehat{S}_{\mathrm{S}}^{\dagger}(\boldsymbol{R}')\,\langle \boldsymbol{R}'|n\rangle\right] \\
&= \sum_{n'} p_{n'}\int dR\int dR'\,\langle n'|\boldsymbol{R}'\rangle\,\langle \boldsymbol{R}|n'\rangle \\
&\quad \times \widehat{S}_{\mathrm{S}}(\boldsymbol{R})\widehat{\rho}_{\mathrm{i}}^{(\mathrm{el})}\widehat{S}_{\mathrm{S}}^{\dagger}(\boldsymbol{R}')\left[\sum_N \langle \boldsymbol{R}'|n\rangle\,\langle n|\boldsymbol{R}\rangle\right] \\
&= \sum_{n'} p_{n'}\int dR\,\langle n'|\boldsymbol{R}\rangle\,\langle \boldsymbol{R}|n'\rangle\,\widehat{S}_{\mathrm{S}}(\boldsymbol{R})\widehat{\rho}_{\mathrm{i}}^{(\mathrm{el})}\widehat{S}_{\mathrm{S}}^{\dagger}(\boldsymbol{R}) \\
&= \int dR\,p(\boldsymbol{R})\widehat{S}_{\mathrm{S}}(\boldsymbol{R})\widehat{\rho}_{\mathrm{i}}^{(\mathrm{el})}\widehat{S}_{\mathrm{S}}^{\dagger}(\boldsymbol{R}).
\end{aligned} \tag{17}$$

In the third row, the completeness relation of the object states

$$\sum_n \langle \boldsymbol{R}'|n\rangle\,\langle n|\boldsymbol{R}\rangle = \delta(\boldsymbol{R}-\boldsymbol{R}') \tag{18}$$

has been used. The diagonality in object coordinates (16) is needed to assure that the subtrace over final object states in (9) can be substituted by the subtrace over object coordinate in (17).

The density matrix calculated in the last row of (17) is equivalent to the quantities calculated by the FP method: The final density matrix of the static case is averaged over initial object positions. It must be stressed that (16) does not correspond to the elastic or coherent scattering subchannel of electron-phonon scattering. The coherent subchannel is given by evaluating (16) for $n \equiv n'$ and the elastic subchannel by summing (16) over final states $n$ without energy losses, i.e., with $\mathcal{E}_n = \mathcal{E}_{n'}$. Both result in different final density matrices than (16), which means that quantities calculated by this method do not correspond to the thermal average purely coherently (or elastically) scattered electrons.

The requirement (C2) relates the validity of the static approximation to the energy transfer due to inelastic scattering between the fast electron and the object and the extents of the object. It should be noted that this relationship in principle also works for other inelastic object excitations. However, for higher energy transfers than in the case of phonon scattering, the static approximation will break down for much smaller objects.

## IV. METHODS

### A. Paraxial ansatz

The scattering matrix ansatz (23) gives a concise framework for a discussion of more general properties of the electron-phonon scattering process. For the numerical evaluation of scattering matrix elements, a paraxial ansatz is chosen, which follows the coupled channels approach of Yoshioka [14]. The joint wave function $|\Psi\rangle$ of electron and object is described by a superposition of paraxial waves:

$$\langle \boldsymbol{r}|\Psi\rangle = \sum_n \varphi_n(\boldsymbol{r}) \exp(i2\pi k_n z)\,|n\rangle\,. \tag{19}$$

The $\varphi_n(\boldsymbol{r})$ are the partial wave fronts corresponding to wave numbers $k_n = k(\mathcal{E}_n + eU_{\mathrm{acc}} - E)$. Only states with conforming total energies are considered here.

Inserting (19) into the relativistically corrected time-independent Schrödinger equation, one eventually arrives at a coupled set of equations [14,36]

$$\begin{aligned}\left[\partial_z^2 + i4\pi k_n \partial_z + \Delta_{xy}\right]\varphi_n(\boldsymbol{r}) \\ = 4\pi^2 \sum_{n'} \exp[i2\pi(k_n - k_{n'})z] U_{nn'}(\boldsymbol{r})\varphi_{n'}(\boldsymbol{r}).\end{aligned} \tag{20}$$

using $k_n - k_{n'} \approx -\frac{\sigma}{2\pi e}(\mathcal{E}_n - \mathcal{E}_{n'})$

Within these equations, the transition potentials are given by

$$U_{nn'}(\boldsymbol{r}) = \frac{2m_0\gamma}{h^2}\,\langle n|V(\boldsymbol{r})|n'\rangle\,, \tag{21}$$

where $\gamma$ is the relativistic correction. Applying the high-energy approximation, i.e., neglecting the second derivative with respect to $z$ in (20), this becomes a set of coupled first-order differential equations:

$$\begin{aligned}\partial_z \varphi_n(\boldsymbol{r}) = \frac{i}{4\pi k_n}\Delta_{xy}\varphi_n(\boldsymbol{r}) \\ - i\frac{\pi}{k_n}\sum_{n'} \exp[i2\pi(k_n - k_{n'})z] U_{nn'}(\boldsymbol{r})\varphi_{n'}(\boldsymbol{r}).\end{aligned} \tag{22}$$

These equations are used to numerically propagate the envelope functions $\varphi_n(\boldsymbol{r})$ through regions of nonvanishing potential.

For rotational symmetric systems, like the model system used in this paper, it suffices to calculate the scattering matrix elements for transitions $n' \to n$ and the $xy$ components of the scattering vector $\boldsymbol{q} = \boldsymbol{k} - \boldsymbol{k}'$:

$$S_{nn'}(q_x, q_y) = \langle \boldsymbol{q} + \boldsymbol{k}', n|\widehat{S}|\boldsymbol{k}', n'\rangle\,. \tag{23}$$

These matrix elements can be obtained from the envelope functions $\varphi_n(\boldsymbol{r})$ in a plane $z_{\mathrm{f}}$ behind the object, as described in Appendix D.

### B. Model object

To investigate the general properties of electron-phonon scattering, we take a simple model object: a single atom at position $\boldsymbol{R}$ in a harmonic three-dimensional potential. The potential simulates the lattice vibrations of the object. The dynamics of the harmonic oscillator are well known [33]:

$$\widehat{H}_{\mathrm{obj}}(\boldsymbol{R}) = \frac{\hbar^2}{2M}\Delta_R + \frac{M\omega^2}{2}R^2. \tag{24}$$

$M$ is the mass of the atom and $\omega$ is the angular frequency of the oscillation. The eigensolutions to the above Hamiltonian are given by the product

$$\langle \boldsymbol{R}|n\rangle \equiv \langle \boldsymbol{R}|n_x n_y n_z\rangle = a_{n_x}(X)a_{n_y}(Y)a_{n_z}(Z)$$

with $\boldsymbol{R} = (X, Y, Z)$ and the object quantum numbers given by the triple $n \equiv n_x n_y n_z$. In the following, these vibration states are referred to as $|n_x n_y n_z\rangle$. The $a_n(\xi)$ are the known solutions for the $n$th eigenstate of the one-dimensional harmonic oscillator

$$a_n(\xi) = \frac{1}{\sqrt{2^n n!}}\left(\frac{M\omega}{\pi\hbar}\right)^{1/4} H_n\left(\sqrt{\frac{M\omega}{\hbar}}\xi\right)\exp\left(-\frac{1}{2}\frac{M\omega}{\hbar}\xi^2\right)$$

with the Hermite polynomials $H_n(\xi)$. The corresponding energies are given by

$$\widehat{H}_{\mathrm{obj}}\,|n_x n_y n_z\rangle = \hbar\omega\left(\tfrac{3}{2} + n_x + n_y + n_z\right)|n_x n_y n_z\rangle\,.$$

The interaction potential between the atom and the fast electron is given by the Coulomb interaction between them. For the scope of this paper, it suffices to assume that this interaction potential is given by the Fourier transformation of the atomic form factor $f_{\mathrm{el}}(\boldsymbol{k})$. In coordinate representation,

$$\widehat{V}(\boldsymbol{r}, \boldsymbol{R}) = e\int_{-\infty}^{+\infty} d^3k\, f_{\mathrm{el}}(\boldsymbol{k})\exp[i2\pi\boldsymbol{k}\cdot(\boldsymbol{r} - \boldsymbol{R})]. \tag{25}$$

Using the $f_{\mathrm{el}}(\boldsymbol{k})$, the transition potential (21) is readily expressed as

$$\begin{aligned}U_{nn'}(\boldsymbol{r}) = \frac{2m_0 e\gamma}{h^2}\int_{-\infty}^{+\infty} d^3k\, f_{\mathrm{el}}(\boldsymbol{k})\exp(i2\pi\boldsymbol{k}\cdot\boldsymbol{r}) \\ \times\,\langle n|\exp(i2\pi\boldsymbol{k}\cdot\widehat{\boldsymbol{R}})|n'\rangle\,.\end{aligned}$$

### C. Numerical evaluation

The high-energy electron scattering equations (22) are numerically propagated using a fourth-order Runge-Kutta scheme. The rest position of the atom was centered in the $xy$ plane. The $xy$ calculation grid consisted out of $192 \times 192$ points and was sampled with 1.0 pm. The Runge-Kutta propagation was performed from $z_{\mathrm{i}} = -150\,\mathrm{pm}$ to $z_{\mathrm{f}} = +150\,\mathrm{pm}$ with a step size of $\delta z = 0.5\,\mathrm{pm}$. The numerical implementation of the Laplace operator was implemented by multiplication with $-4\pi^2k^2$ in Fourier space.

Calculations were performed for an acceleration voltage of $U_{\mathrm{acc}} = 200\,\mathrm{kV}$. A single atom of various elements was used as object. Unwise otherwise mentioned the reported results were obtained for a Gold atom.

The oscillator angular frequency $\omega$ was always chosen such that the mean square displacements in thermal average at a temperature of 300 K correspond to a Debye-Waller factor of $B = 0.005\,\mathrm{nm}^2$ (see Ref. [34] for derivation):

$$B = 4\frac{\hbar\pi^2}{M\omega}\coth\left(\frac{\hbar\omega\beta}{2}\right).$$

Here $M$ corresponds to the atom's mass. The corresponding angular frequencies are shown in Table I.

The form factor parametrization of Ref. [37] was chosen for $f_{el}(\boldsymbol{k})$, mainly since the parametrization as sum of Gaussians allowed for efficient calculations of the transition potential $U_{nn'}(\boldsymbol{r})$. However, this parametrization is not fully accurate for scattering angles $|\boldsymbol{q}| > 120\,\mathrm{nm}^{-1}$. It is assumed the general findings are valid nevertheless; however, they might be inaccurate for large angles in a comparison with experimental results.

For the propagation of the equation set (22), always a plane wave along the $z$ axis was chosen as an initial condition of the fast electron with a wave number corresponding to 200 keV energy, i.e., $\boldsymbol{k}_\mathrm{i} = K\boldsymbol{e}_z$. For initial conditions of the object, an eigenstate $|n_\mathrm{i}\rangle$ was chosen. Accordingly, the initial partial waves of the joint system are given by

$$\varphi_n(x, y, z_\mathrm{i}) = \delta_{nn_\mathrm{i}}. \tag{26}$$

As the numerical effort increases with the number of states considered in the propagation, the calculations were restricted to states with quantum numbers

$$n_x + n_y + n_z \leqslant 5$$

corresponding to all object energies up to a cutoff energy of

$$\mathcal{E}_n \leqslant \hbar\omega\left(5 + \tfrac{3}{2}\right). \tag{27}$$

### D. Approximations

The paraxial ansatz allows calculation of the scattering amplitudes, i.e., the elements of the $S$ matrix, with minimal additional assumptions. This is possible since the investigated model system is rather simple. For larger systems, this ansatz is most likely not numerically feasible anymore, and thus further inelastic scattering approximations must be made.

However, having the solutions of the paraxial ansatz allows the investigation of how good commonly applied further approximations are.

#### *1. Bethe approximation*

The phonon dynamics usually are treated as small atomic displacements $\boldsymbol{u}$ with respect to the atom's rest positions $\boldsymbol{R}_0$, i.e., $\boldsymbol{R} \equiv \boldsymbol{R}_0 + \boldsymbol{u}$. The transition potential (21) can be developed in a Taylor series expansion with respect to $\widehat{\boldsymbol{u}}$:

$$\begin{aligned} U_{nn'}(\boldsymbol{r}) &= \frac{2m_0\gamma}{h^2}\,\langle n|V(\boldsymbol{r}, \boldsymbol{R}_0 + \widehat{\boldsymbol{u}})|n'\rangle \\ &= \frac{2m_0\gamma}{h^2}[\langle n|n'\rangle\, V(\boldsymbol{r}, \boldsymbol{R}_0) + \langle n|\widehat{\boldsymbol{u}}|n'\rangle \cdot \nabla_R V|_{\boldsymbol{R}=\boldsymbol{R}_0} \\ &\quad + (\langle n|\widehat{\boldsymbol{u}}|n'\rangle \cdot \nabla_R)^2 V|_{\boldsymbol{R}=\boldsymbol{R}_0} + \cdots]. \end{aligned} \tag{28}$$

The approximation is the truncation of this series after the first order [11,12,27] or second order in $\boldsymbol{u}$ [29]. This approximation has the numerical advantage that $\langle n|\widehat{\boldsymbol{u}}|n'\rangle$ is usually easy to calculate, while the calculation of $\langle n|V(\boldsymbol{r}, \boldsymbol{R}_0 + \widehat{\boldsymbol{u}})|n'\rangle$ requires far more effort. This becomes especially important if the lattice vibrations are investigated in a full phonon model with correlative atom vibrations, instead of a model where the vibrations of each atom are treated independently.

An alternative form to this approximation also found in literature is the use of the thermally averaged potential instead of the static potential in (28) [18,19,38].

This approximation is quite common in calculations of electron-phonon interaction. In Ref. [39], it is named the "Bethe approximation" and it indeed can be found in Bethe's work [40]. The first order of this approximation is also referred to as dipole approximation, e.g., in Ref. [30]. However, the term "Bethe approximation" is here used in lack of a better name and should be used with care in a broader context, since several distinct and unrelated approximations carry this name.

#### *2. Projection approximation*

The set of first-order differential equations (22) can be calculated using a coupled-channel multislice formalism. Within a multislice formulation, Eqs. (22) are approximately propagated for a thin slice of sufficiently small thickness and this propagation step is repeated until the solution at the exit plane of the specimen is reached.

For a single slice and an object being initially in an eigenstate $n'$, the envelope functions belonging to noninitial object states $n \neq n'$ are given by

$$\begin{aligned} \varphi_n(x, y, z) &= -i\frac{\pi}{k_n}\int_{-\infty}^{+\infty} dz\, \exp[i2\pi(k_n - k_{n'})z]U_{nn'}(x, y, z) \\ &\approx -i\frac{\pi}{k_n}\int_{-\infty}^{+\infty} dz\, U_{nn'}(x, y, z). \end{aligned} \tag{29}$$

For the relevant energy losses and typical slice thickness, the phase factor in (29) can be neglected. Similar formulations can be found in Refs. [19,27,34].

TABLE I. Angular frequencies for used atom elements.

| Element | $\omega$ (rad/s) | Energy quanta $\hbar\omega$ (meV) | Cutoff energy $(5 + \frac{3}{2})\hbar\omega$ (meV) |
|---|---|---|---|
| C | $62.9 \times 10^{12}$ | 41.4 | 268.9 |
| Si | $39.0 \times 10^{12}$ | 25.6 | 166.6 |
| Cu | $25.3 \times 10^{12}$ | 16.7 | 108.3 |
| Ag | $19.3 \times 10^{12}$ | 12.7 | 82.6 |
| Au | $14.2 \times 10^{12}$ | 9.4 | 60.8 |

## V. RESULTS

### A. Scattering amplitudes

For a particular state transition $|n'\rangle \to |n\rangle$, the $S$-matrix elements $S_{nn'}(q_x, q_y)$ describe the complex scattering amplitudes for elastic and inelastic transitions in diffraction space. When the $S$-matrix elements are inversely Fourier transformed with respect to the electron scattering vector, the corresponding partial wave fronts $\mathcal{F}^{-1}[S_{nn'}](x, y)$ of the electron after the respective state transitions are obtained in real space.

The central part of the partial wave fronts is displayed in Fig. 1 for selected transitions. The rest position of the

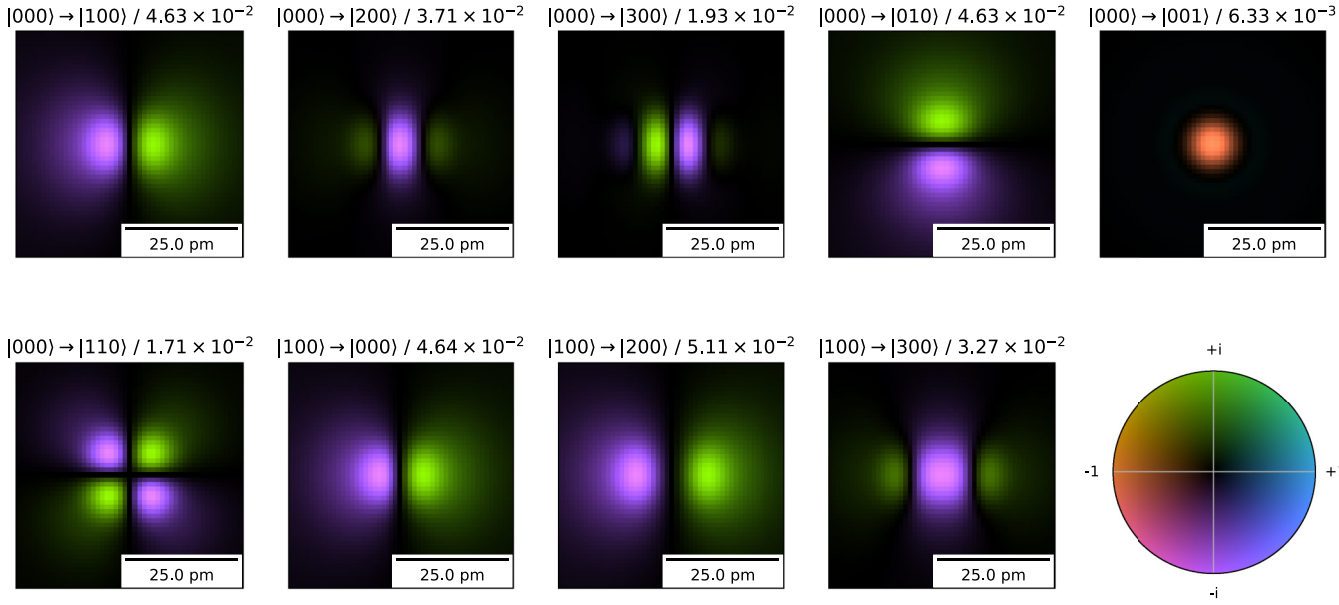


FIG. 1. Electron partial wave fronts after selected state transition. The corresponding color map is shown in the lower right corner. The complex-valued partial wave fronts are scaled differently to accommodate for the observed modulus range. The scaling factor is denoted above the plots.

electron is in the center of the displayed region. The color map in the lower right corner of Fig. 1 is used to display the complex values of the partial wave fronts. For display, the values of the wave fronts have been scaled such that their maximal modulus is equal to unity and the complex values can be shown using a common color map. The scaling factor is indicated above the individual displays. The incident beam was normalized to exhibit a homogeneous modulus of one.

With increasing number of phonon excitations and annihilations, the transitions become less probable. Transitions, which excite vibrations in beam direction, e.g., $|000\rangle \rightarrow |001\rangle$, also have nonvanishing probabilities but are far less probable in comparison.

Note that the modulus squared scattering amplitudes for transitions $|000\rangle \rightarrow |100\rangle$ and $|100\rangle \rightarrow |000\rangle$ are identical due to

$$U_{nn'}(\boldsymbol{r}) = U^*_{n'n}(\boldsymbol{r}) = U_{n'n}(\boldsymbol{r}).$$

The second equality is due to the $U_{nn'}(\boldsymbol{r})$ being real valued, since the eigenfunction of the three-dimensional (3D) harmonic oscillator are real valued.

The partial wave fronts for the coherent subchannels $|n'\rangle \rightarrow |n'\rangle$, where the object did not undergone a state transitions are shown in Fig. 2. Since the variations of the wave fronts are too small to be noticeable when displayed using a color map like in Fig. 1, the amplitudes and phases of the fronts are displayed separately. The phases strongly resemble the projections of the 3D oscillator's probability density convoluted by the atomic potential, as expected since the gold atom can also be approximated as a weak phase object. In contrast to the phases, the amplitudes are less blurred. Here, the contrast is caused primarily by electrons being scattered into the incoherent subchannels. This also explains the increased amplitude in the center of the $|000\rangle \rightarrow |000\rangle$ transition: The electrons passing close to the nucleus are exciting a larger number of phonons; these transitions, however, are not included in the calculation because of used the energy cutoff. With increasing cutoff energy, this effect becomes smaller (not shown here).

Within the literature, the approximation $U_{nn} \approx U_{00}$ (for all $n$) is used in previous works, which investigate the correctness of the frozen phonon method [31,32]. Comparing the results in Fig. 2 for $|000\rangle \rightarrow |000\rangle$ and $|100\rangle \rightarrow |100\rangle$ clearly shows that this equivalence is not necessarily given.

Obviously, the simple model presented here only allows calculation of inelastic scattering amplitudes for a single vibrating atom. For realistic scattering cross sections and EELS spectra of extended specimens, it is additionally necessary to consider the correlated vibrations and associated phonon dispersion relations instead of relying on a simple Einstein model. Calculated transition potentials for correlated phonon vibrations can be found for instance in the works of Martin *et al.* [15] and Forbes *et al.* [20].

### B. Scattering cross sections

For a particular state transition $|n'\rangle \rightarrow |n\rangle$, the scattering probabilities for this transition, i.e., the scattering cross sections, are given by the modulus square of the transition elements $S_{nn'}(q_x, q_y)$. Cross sections for specific energy losses can be calculated from this. Figure 3 shows the azimuthally averaged scattering cross sections for a single gold atom initially in the ground state, i.e., $|n'\rangle = |000\rangle$. The cross section for a specific energy loss $\Delta E$ is here calculated as

$$\sum_{n|\mathcal{E}_n - \mathcal{E}_{n'} = \Delta E} \frac{1}{2\pi q} \int_0^{2\pi} d\vartheta \, \|S_{nn'}(q\cos\vartheta, q\sin\vartheta)\|^2. \qquad (30)$$

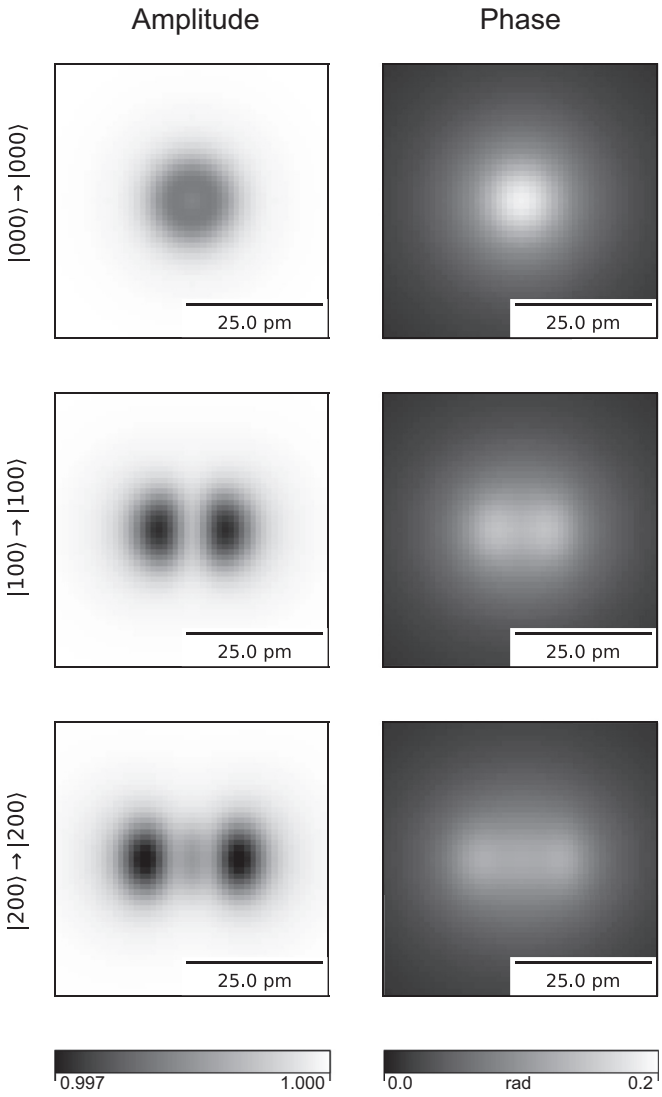


FIG. 2. Selected electron partial waves for coherent state transitions. The amplitudes are shown on the left-hand side with the corresponding phases on the right-hand side.

Azimuthally averaged total, inelastic, and incoherent cross sections can be calculated accordingly using the definitions of Sec. II C. For a gold atom, it can be found that for scattering angles larger than ≈94 mrad most of the scattered intensity is scattered inelastically. With increasing energy loss $\Delta E$, the average scattering angles become larger and the total scattering cross section becomes smaller.

The elastic and inelastic scattering cross sections for a thermal average of initial states for the gold atom are displayed in Fig. 4. One observes that for higher temperature the smallest scattering angle where inelastic scattering prevails decreases, from ≈94 mrad at 0 K, over ≈73 mrad at 100 K, to ≈61 mrad at 300 K. Also a significant dependence of the scattering cross sections at larger angles on the temperature is found. For 200 mrad, the 300 K cross section is roughly half as intense as at 0 K, while at 50 mrad the 300-K cross section is only 10% less than the 0-K cross section.

Another noteworthy observation is the change in the scattering amplitudes with increasing temperature in the coherent

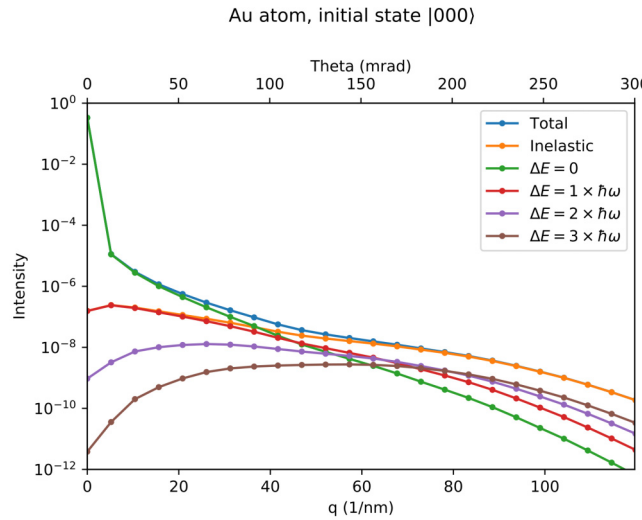


FIG. 3. Azimuthally averaged scattering cross sections for a gold atom initially in state |000⟩.

subchannels, e.g., at 100 mrad for gold [Fig. 4(b)]. This is the effect of an mixed initial object state (Huang scattering) [41]. It shows that scattering due to a mixed initial state (i.e., thermal diffuse scattering for crystalline objects) also occurs in the coherent subchannel and thus is not solely an effect of incoherent-inelastic scattering. At higher temperature, this Huang scattering becomes stronger with temperature for higher scattering angles (for gold >200 mrad), while at lower angles it even decreases the scattering cross sections slightly. Nevertheless, the incoherent scattering for most higher angular ranges is stronger by one order of magnitude or more.

Since the phonon energies and the strength of the atom's electrostatic potential vary strongly with the mass and atom number, the scattering cross sections were also calculated for various elements and are shown in Fig. 5. As expected, the cross sections strongly depend on the atom number. The cross over between angles where most electrons are scattered elastically versus inelastically increases with atom number from ≈40 mrad for carbon, over ≈43 mrad for silicon, ≈50 mrad for copper, ≈55 mrad for silver, and up to ≈61 mrad for gold.

### C. Static *S*-matrix approximation

If the static scattering matrix approximation (15) and accordingly (16) are correct, the two quantities

$$\sum_n \|S_{nn'}(q_x, q_y)\|^2 \approx \int dR \|\langle \boldsymbol{R}|n'\rangle\|^2 \|S_S(\boldsymbol{R}; q_x, q_y)\|^2$$

should be approximately equal for any initial state $|n'\rangle$. On the left-hand side, the cross sections are summed over final states, and on the right-hand side, the static cross section is summed over object coordinates. In Fig. 6, both quantities are shown after azimuthal averaging for a gold atom and different cutoff energies (27) using the initial state $|n'\rangle = |000\rangle$.

The cross sections summed over final states approaches the static cross section with increasing cutoff energy. This

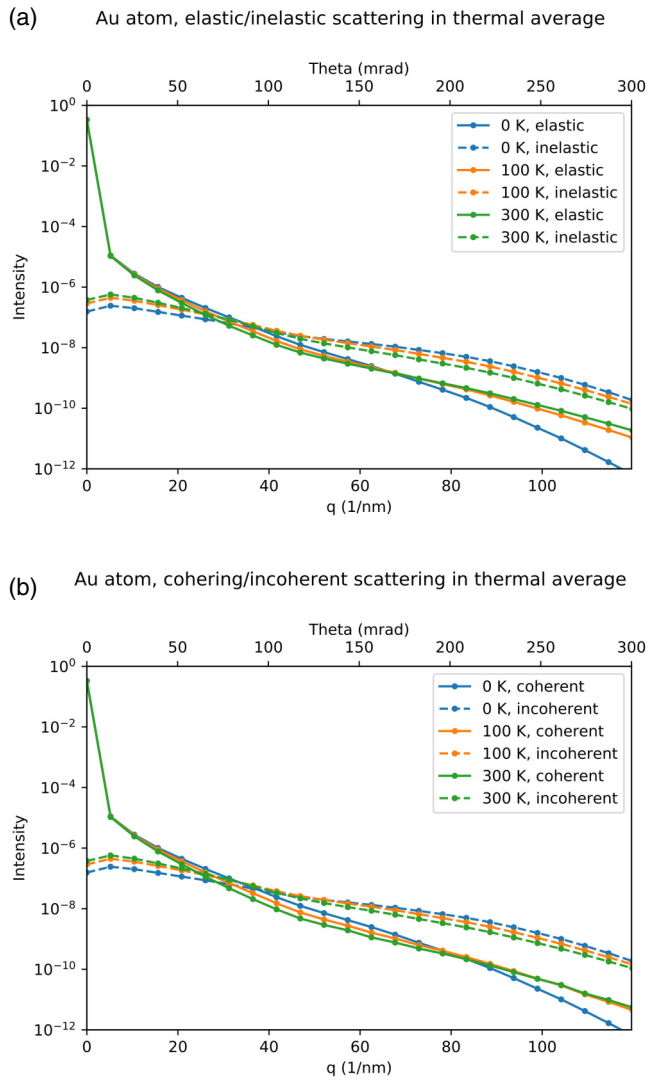


FIG. 4. (a) Elastic and inelastic cross sections. (b) Coherent and incoherent cross sections. Both are for a gold atom in thermal average.

shows that the remaining difference between the summed cross sections and the static cross section are due to the completeness relation (18) not being completely fulfilled, since the cutoff energy is finite in the present calculations. In any case, the cross sections $\Theta < 200\,\text{mrad}$ should be correct for $\mathcal{E}_n \leqslant (5+\frac{3}{2})\hbar\omega$.

It should noted the findings of Sec. V B are still valid even for higher scattering angles ($200\,\text{mrad} < \Theta < 300\,\text{mrad}$), since we found that a change in the cutoff energy (27) does not change the results presented in Fig. 4 significantly (not shown here).

The elastic cross section is also plotted in Fig. 6 as given by (30) for $\Delta E = 0$. It is obvious in comparison to the static cross section that both cross sections are different entities and must not be thought of as equal. Even if no state transitions within a simulation with fixed atom positions are considered, such a simulation does not represent the elastic or coherent subsector of phonon scattering.

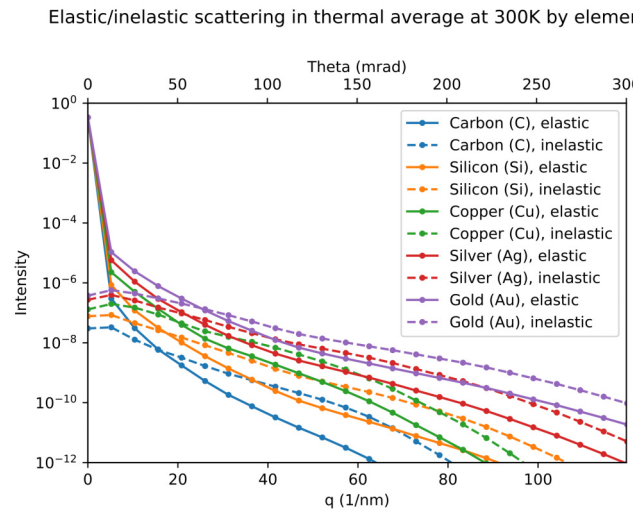


FIG. 5. Thermally and azimuthally averaged scattering cross sections for various elements at 300 K.

### D. Inelastic scattering approximations

The paraxial ansatz allows to calculate the scattering amplitudes, i.e., the elements of the $S$ matrix, with minimal additional assumptions. This allows investigation of how good further approximations are. Specifically, the following approximations are tested:

(1) The Bethe approximation (28) in first and second orders.

(2) The first-order Bethe approximation for the thermally averaged potential. The thermally averaged potential is implemented by including the Debye-Waller factor $\exp(-Bk^2/4)$ within the integral in (25).

(3) The projection approximation (29).

(4) Integration of the static approximation according to (16) by means of the Monte Carlo method. In total,

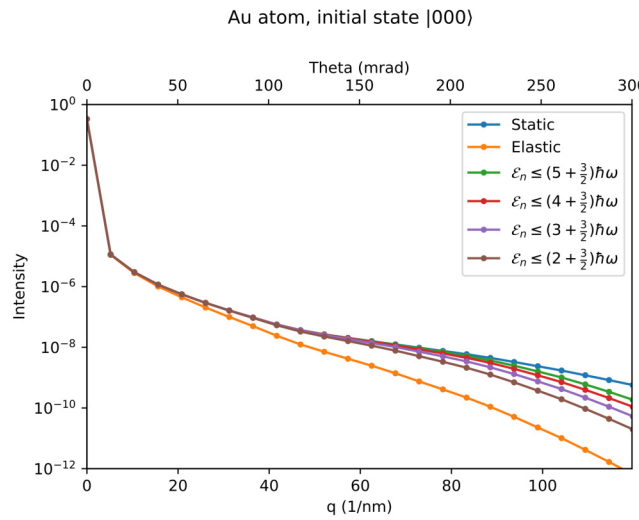


FIG. 6. Comparison of static scattering cross section with cross sections summed over object states in dependence of energy cutoff. Additionally, the cross section for elastic scattering is displayed for comparison.

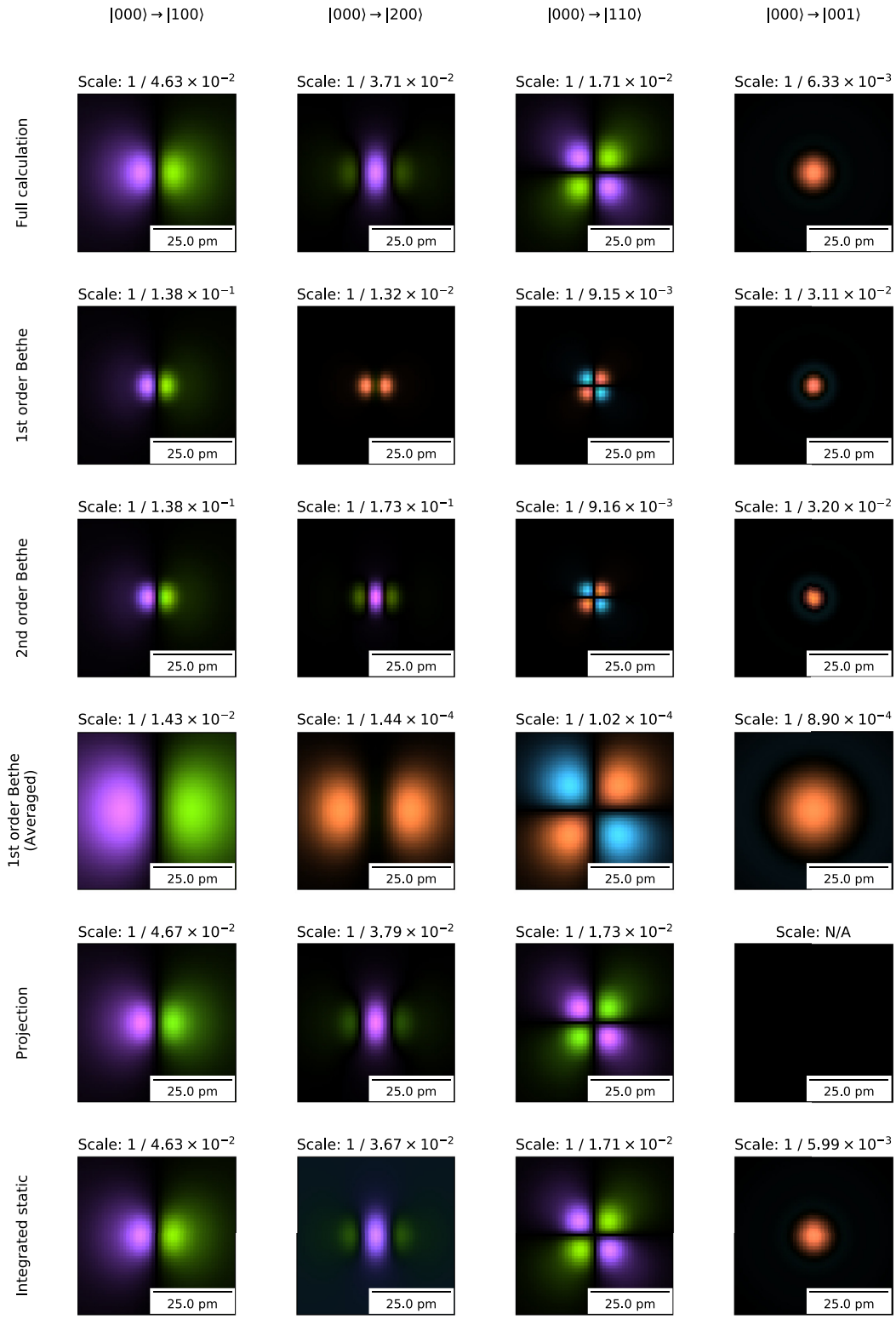


FIG. 7. Comparison of scattering amplitudes for selected transitions (columns) using various approximations of inelastic scattering (rows). The first row shows the result of the full calculation. See the lower right corner of Fig. 1 for color map. Note the varying scale of the complex values above the displays.

1 million atom positions were uniformly sampled within $\pm 9\sqrt{\hbar/\omega M}$ of the rest position, and for each atom position also the positions mirrored along the $x$, $y$, and $z$ axes were sampled.

Figure 7 shows the scattering amplitudes for selected inelastic transitions. The discussed findings can be observed on all investigated transitions, although only some transitions are shown here.

While the Bethe approximation reflects the general structure of the scattering amplitudes as long as the number of excited phonons is less equal to the approximation's order, their spatial extents and magnitude are severely different from the full solution. The calculated transition probabilities in the approximation are roughly one magnitude larger than in the full calculation (see, e.g., first-order Bethe approximation for transition $|000\rangle \rightarrow |100\rangle$ or the second-order Bethe approximation for the transition $|000\rangle \rightarrow |200\rangle$). This has effects on higher order scattering: For instance, within the first-order Bethe approximation, the transition probability for the excitation of more than one phonon is zero, which forbids a direct $|000\rangle \rightarrow |200\rangle$ transition. However, since the first Born order transition (single scattering) within this approximation is so strong, the second Born order transition (double scattering) becomes relevant (see $|000\rangle \rightarrow |200\rangle$ transitions for first-order Bethe approximation in Fig. 7). Obviously, being a multiple scattering effect, the phases of this approximated transition become unrealistic. For the second-order Bethe approximation, the single scattering for $|000\rangle \rightarrow |200\rangle$ is much stronger, masking this effect. Quite the opposite is found for the (first-order) Bethe approximation of the thermally averaged potential: This approximation strongly underestimates the magnitudes of the amplitudes, while the extents are far more extended than in the full calculation.

The $m$th-order term of a Bethe approximation can also be interpreted as a $m$-phonon process [42]. However, even for the excitation of a single phonon, also the creation and annihilation of virtual phonons must be taken into account: For example, the $|000\rangle \rightarrow |100\rangle$ transition also occurs in the three-phonon process, where the $|100\rangle$ phonon is created, followed by annihilation and recreation. Other virtual phonon processes are permutations thereof or appear in higher (odd) order phonon processes [43]. This may explain the deviations between the full model and the first-order Bethe approximation observed here. A further discussion of such virtual inelastic scattering effects on the scattering potential can be found in Ref. [44] and a discussion of its temperature influence is in Ref. [45].

For transitions which excite vibrations transverse to the beam direction like $|000\rangle \rightarrow |100\rangle$ and $|000\rangle \rightarrow |200\rangle$, the projection approximation is well fulfilled. Longitudinal vibrations cannot be represented with this approximation, since the projection integral over the the corresponding matrix elements evaluates as zero. However, the transition probability for the longitudinal vibrations is two orders below the probability of transverse transitions, rendering the importance of longitudinal transitions negligible in comparison. It should be noted that the remaining differences between the projected scattering amplitudes and those of the full calculation might be also rooted in the assumption of a weak phase object, which might be better fulfilled for lighter elements than a gold atom.

The integration of the static approximation gives in general very reliable scattering amplitudes in magnitude, general structure, as well as spatial extent. Found deviations are caused by an insufficiently accurate evaluation of the integral: The symmetrization of sampling positions keeps the integrals of energy losses corresponding to even multiples of $\hbar\omega$ accurate, while accurate determination of odd multiples requires a correct evaluation of the tails of the vibrational wave functions. Especially toward higher energy losses the accuracy of the numerical integration becomes critical, since the magnitude of the amplitudes become smaller and the absolute errors of the integration become more relevant.

## VI. CONCLUSION

A rigorous quantum mechanical proof within the scattering matrix framework is presented, showing that phonon-related transition probabilities can be approximated by integration over results obtained by conventional simulation methods with static atom positions. The approximation holds for multiple scattering as well as correlated vibrations of the atoms within the object. The requirement for this approximation relates the inelastic energy losses of the fast electron to the extent of the specimen. For typical phonon energy ranges and specimen thicknesses used for HAADF imaging, averaging TEM calculations for fixed atom positions over the position's probability density (as done in the frozen phonon method) will yield the correct results. However, all electrons regardless of the energy loss must be registered without any distortions, e.g., caused by chromatic aberrations.

The scattering matrix elements for phonon transitions of a simple model, a single atom in a harmonic potential, were calculated. Combining the scattering matrix elements allows the calculation of elastic, coherent, inelastic, incoherent, and total cross sections and their thermal average. It is found that the electrons scattered into high angles are predominantly scattered due to inelastic phonon scattering and not due to thermal averaging. For a single gold atom and electrons with 200 keV acceleration energy, inelastic scattering prevails $>61$ mrad at temperature of 300 K. For lighter elements, slightly smaller threshold angles are found.

Several commonly used approximations for calculation of phonon transition matrix elements were tested. For the expansion of the object potential into a power series of displacements, it is found that virtual inelastic scattering must be taken into account for inelastic scattering cross sections, at least for a scattering at a single atom. Correct results are found for approximations, which project the transition elements over the thickness of typical slices within the multislice method.

## ACKNOWLEDGMENT

The author thanks Axel Lubk for valuable discussions on the topic and Michael Lehmann for reading of the manuscript.

## APPENDIX A: *S* MATRIX

This Appendix describes how $S$-matrix elements can be calculated by use of the Green's operator. For a full treatment of the underlying quantum mechanical scattering theory, the reader is referred to the literature [35,39].

The Green's operator for the asymptotic Hamiltonian $\widehat{H}_0$ (3) is given by

$$\widehat{G}_0(E) = \lim_{\epsilon \to 0^+} \frac{1}{E - \widehat{H}_0 + \mathrm{i}\epsilon}.$$

It should be noted that this operator explicitly depends on the energy of the whole system. The operator is readily written

down in its spectral representation

$$\widehat{G}_0(E) = \lim_{\epsilon\to 0^+} \int d^3k \sum_n \frac{1}{E - \mathcal{E}_{\boldsymbol{k},n} + \mathrm{i}\epsilon} \, |\boldsymbol{k}, n\rangle \, \langle \boldsymbol{k}, n|,$$

where $\mathcal{E}_{\boldsymbol{k},n}$ is the energy of $|\boldsymbol{k}, n\rangle$ . Its coordinate representation can be written using the well-known Green's function of the free electron:

$$\langle \boldsymbol{r}|\widehat{G}_0(E)|\boldsymbol{r}'\rangle = -\frac{2\pi m_0}{h^2} \sum_n \frac{\exp(i2\pi k(E_n + eU - E)|\boldsymbol{r} - \boldsymbol{r}'|)}{|\boldsymbol{r} - \boldsymbol{r}'|} \, |n\rangle \, \langle n|. \tag{A1}$$

For scattering in the full system, as described by $\widehat{H}$, the $S$-matrix element giving the scattering amplitude from a state $|\boldsymbol{k}', n'\rangle$ into a state $|\boldsymbol{k}, n\rangle$ on the energy shell is given by

$$\langle \boldsymbol{k}, n\widehat{S}|\boldsymbol{k}', n'\rangle = \langle \boldsymbol{k}, n|\boldsymbol{k}', n'\rangle - 2\pi i \, \langle \boldsymbol{k}, n|\widehat{T}|\boldsymbol{k}', n'\rangle \, . \tag{A2}$$

Above, we made use of the $T$ matrix, which can be iterated by a Born series using $\widehat{G}_0(E)$:

$$\langle \boldsymbol{k}, n|\widehat{T}|\boldsymbol{k}', n'\rangle = \sum_m \langle \boldsymbol{k}, n|[\widehat{V}\widehat{G}_0(E)]^m\widehat{V}|\boldsymbol{k}', n'\rangle \, . \tag{A3}$$

Single scattering is described by keeping only the first-order term of this series:

$$\langle \boldsymbol{k}, n|\widehat{T}_1|\boldsymbol{k}', n'\rangle = \langle \boldsymbol{k}, n|\widehat{V}|\boldsymbol{k}', n'\rangle \, . \tag{A4}$$

This results in the single scattering (first-order) $S$ matrix

$$\langle \boldsymbol{k}, n|\widehat{S}_1|\boldsymbol{k}', n'\rangle = \langle \boldsymbol{k}, n|\boldsymbol{k}', n'\rangle - 2\pi i \, \langle \boldsymbol{k}, n|\widehat{V}|\boldsymbol{k}', n'\rangle \, . \tag{A5}$$

In the literature, often an additional $\delta$ distribution is found in (A2), which ensures energy conservation. This factor is omitted here for clarity. In this paper, the elements of the $S$ matrix will only be evaluated for initial and final states with same total total energy, and thus the energy conservation is always given.

## APPENDIX B: $S$ MATRIX FOR STATIC APPROXIMATION

The $S$ matrix for the static case can be formulated similar to the full case in Appendix A with the free electron's Hamiltonian as asymptotic case. In the static approximation, the electron's energy is always given by its acceleration energy $eU_{\mathrm{acc}}$. The Green's operator for the free electron is given by

$$\langle \boldsymbol{r}|\widehat{G}_{\mathrm{S},0}|\boldsymbol{r}'\rangle = -\frac{2\pi m_0}{h^2} \frac{\exp(i2\pi K|\boldsymbol{r} - \boldsymbol{r}'|)}{|\boldsymbol{r} - \boldsymbol{r}'|}. \tag{B1}$$

The elements of the $S$- and $T$-matrices are

$$\langle \boldsymbol{k}'|\widehat{S}_{\mathrm{S}}(\boldsymbol{R})|\boldsymbol{k}\rangle = \langle \boldsymbol{k}|\boldsymbol{k}'\rangle - 2\pi i \, \langle \boldsymbol{k}|\widehat{T}_{\mathrm{S}}(\boldsymbol{R})|\boldsymbol{k}'\rangle \, , \tag{B2}$$

$$\langle \boldsymbol{k}'|\widehat{T}_{\mathrm{S}}(\boldsymbol{R})|\boldsymbol{k}\rangle = \sum_m \langle \boldsymbol{k}|[\widehat{V}_{\mathrm{S}}(\boldsymbol{R})\widehat{G}_{\mathrm{S},0}]^m\widehat{V}_{\mathrm{S}}(\boldsymbol{R})|\boldsymbol{k}'\rangle \, . \tag{B3}$$

Single scattering is described by keeping only the first term of the Born series in (B2):

$$\langle \boldsymbol{k}|\widehat{T}_{\mathrm{S},1}(\boldsymbol{R})|\boldsymbol{k}'\rangle = \langle \boldsymbol{k}|\widehat{V}_{\mathrm{S}}(\boldsymbol{R})|\boldsymbol{k}'\rangle \, . \tag{B4}$$

## APPENDIX C: EQUIVALENCE OF $S$ MATRICES

Comparing the first elements of the Born series of the $T$ matrix of the full treatment (A4) and the static case (B4) shows their equivalence for the single scattering case

$$\begin{aligned}\langle \boldsymbol{R}|\widehat{T}_1|\boldsymbol{R}'\rangle &= \langle \boldsymbol{R}|\widehat{V}|\boldsymbol{R}'\rangle = \widehat{V}(\boldsymbol{R}) \, \langle \boldsymbol{R}|\boldsymbol{R}'\rangle = \widehat{V}_{\mathrm{S}}(\boldsymbol{R}) \, \langle \boldsymbol{R}|\boldsymbol{R}'\rangle \\ &= \widehat{T}_{\mathrm{S},1}(\boldsymbol{R}) \, \langle \boldsymbol{R}|\boldsymbol{R}'\rangle \, ,\end{aligned} \tag{C1}$$

due to (2) and (14). In order to show the equivalence also for higher order terms (multiple scattering) an approximation of the Green's operator is needed.

The Green's operator (A1) for the full inelastic scattering problem will only be evaluated in a product between $V(\boldsymbol{r}, \boldsymbol{R})$ and $V(\boldsymbol{r}', \boldsymbol{R}')$; see (A3). But the interaction potential $V(\boldsymbol{r}, \boldsymbol{R})$ will only be nonzero in the area of the specimen. For a given specimen size of $A$, this means only terms of the Green's operator with $|\boldsymbol{r} - \boldsymbol{r}'| < 2A$ must be considered.

The energy spread of the relevant object states $|n\rangle$ for phonon scattering (a few meV) will be small compared to the electron energy (a few hundred keV). Here, the energy spread of the object states is given by the energy changes of the object due to inelastic scattering and due to the spread of initial states due to thermal excitation.

In the exponential of the Green's operator (A1), only the product of $|\boldsymbol{r} - \boldsymbol{r}'|$ and the wave number appears. For an object energy deviation from the mean object energy of $\Delta E_n = \mathcal{E}_n + eU - E$, these wave number will change by $\Delta k_n = \frac{\sigma}{2\pi e}\Delta E_n$ from $K$ as given by (5). As example, an energy deviation of $\Delta E_n = 100$ meV (which would be rather large for a phonon excitation) changes the wave number of a 100-keV electron by $\Delta k_n = 147\,\mathrm{mm}^{-1}$, which is a million times smaller than the original wave number $K = 270\,\mathrm{nm}^{-1}$. For a $A = 100$ nm large specimen, this means $\Delta k_n|\boldsymbol{r} - \boldsymbol{r}'| < 2A\Delta k_n < 0.03$. However, this is a rather extreme example; most relevant energy changes will be smaller. Thus, for sufficient small wave vector changes $\Delta k_n$ and sufficient small specimen extents $A$

$$2A\Delta k_n \ll 1, \tag{C2}$$

the spherical wave part of the Green's operator can be approximated by

$$\frac{\exp(i2\pi(K + \Delta k_n)|\boldsymbol{r} - \boldsymbol{r}'|)}{|\boldsymbol{r} - \boldsymbol{r}'|} \approx \frac{\exp(i2\pi K|\boldsymbol{r} - \boldsymbol{r}'|)}{|\boldsymbol{r} - \boldsymbol{r}'|}.$$

Using this approximation for the Green's operator (A1) gives

$$\begin{aligned}&\langle \boldsymbol{r}, \boldsymbol{R}|\widehat{G}_0|\boldsymbol{r}', \boldsymbol{R}'\rangle \\ &= -\frac{2\pi m_0}{h^2} \sum_n \frac{\exp(i2\pi(K + \Delta k_n)|\boldsymbol{r} - \boldsymbol{r}'|)}{|\boldsymbol{r} - \boldsymbol{r}'|} \, \langle \boldsymbol{R}|n\rangle \, \langle n|\boldsymbol{R}'\rangle \\ &\approx -\frac{2\pi m_0}{h^2} \frac{\exp(i2\pi K|\boldsymbol{r} - \boldsymbol{r}'|)}{|\boldsymbol{r} - \boldsymbol{r}'|} \sum_n \langle \boldsymbol{R}|n\rangle \, \langle n|\boldsymbol{R}'\rangle \\ &= -\frac{2\pi m_0}{h^2} \frac{\exp(i2\pi K|\boldsymbol{r} - \boldsymbol{r}'|)}{|\boldsymbol{r} - \boldsymbol{r}'|} \, \langle \boldsymbol{R}|\boldsymbol{R}'\rangle \\ &= \langle \boldsymbol{r}'|\widehat{G}_{\mathrm{S},0}|\boldsymbol{r}\rangle \, \langle \boldsymbol{R}|\boldsymbol{R}'\rangle \, ,\end{aligned} \tag{C3}$$

which corresponds to the Green's operator for the static scattering case (B1). When the terms of the full $T$-matrix (A3) are

evaluated in object coordinate representation,

$$\langle \boldsymbol{R}|\widehat{T}|\boldsymbol{R}'\rangle = \sum_m \langle \boldsymbol{R}|(\widehat{V}\widehat{G}_0)^m\widehat{V}|\boldsymbol{R}'\rangle\,. \tag{C4}$$

The equivalence of the $m = 0$ term was already shown above in (C1). For terms with $m > 0$,

$$\begin{aligned}
&\langle \boldsymbol{R}|(\widehat{V}\widehat{G}_0)^m\widehat{V}|\boldsymbol{R}'\rangle \\
&= \int dR'' \int dR''' \langle \boldsymbol{R}|\widehat{V}|\boldsymbol{R}'''\rangle\, \langle \boldsymbol{R}'''|\widehat{G}_0|\boldsymbol{R}''\rangle \langle \boldsymbol{R}''|(\widehat{V}\widehat{G}_0)^{m-1}\widehat{V}|\boldsymbol{R}'\rangle \\
&= \widehat{V}_{\mathrm{S}}(\boldsymbol{R}) \int dR''\, \langle \boldsymbol{R}|\widehat{G}_0|\boldsymbol{R}''\rangle\, \langle \boldsymbol{R}''|(\widehat{V}\widehat{G}_0)^{m-1}\widehat{V}|\boldsymbol{R}'\rangle \\
&\approx \widehat{V}_{\mathrm{S}}(\boldsymbol{R})\widehat{G}_{\mathrm{S},0}\, \langle \boldsymbol{R}|(\widehat{V}\widehat{G}_0)^{m-1}\widehat{V}|\boldsymbol{R}'\rangle,
\end{aligned} \tag{C5}$$

where in the second line the definition (14) and in the third line the approximation (C3) were used. By repeated application of (C5) and eventually due to (C1), it follows for all $m$

$$\begin{aligned}
\langle \boldsymbol{R}|\widehat{T}|\boldsymbol{R}'\rangle &= \langle \boldsymbol{R}|(\widehat{V}\widehat{G}_0)^m\widehat{V}|\boldsymbol{R}'\rangle \approx [\widehat{V}_{\mathrm{S}}(\boldsymbol{R})\widehat{G}_{\mathrm{S},0}]^m\widehat{V}_{\mathrm{S}}(\boldsymbol{R})\, \langle \boldsymbol{R}|\boldsymbol{R}'\rangle \\
&= \widehat{T}_{\mathrm{S}}(\boldsymbol{R})\, \langle \boldsymbol{R}|\boldsymbol{R}'\rangle
\end{aligned}$$

and thus

$$\langle \boldsymbol{R}|\widehat{S}|\boldsymbol{R}'\rangle \approx \widehat{S}_{\mathrm{S}}(\boldsymbol{R})\, \langle \boldsymbol{R}|\boldsymbol{R}'\rangle\,. \tag{C6}$$

It should be noted that for a $N$-times scattering, the Green's operator approximation (C3) is applied $(N-1)$ times. Thus, the requirement (C2) becomes

$$2A\Delta k \ll \frac{1}{N-1}$$

for $N$-times scattering.

## APPENDIX D: SCATTERING MATRIX ELEMENTS FROM PARAXIAL ANSATZ

The scattering matrix elements $S_{nn'}(q_x, q_y)$ are calculated for given transitions $n' \to n$ and $xy$ components of the scattering vector $\boldsymbol{q} = \boldsymbol{k} - \boldsymbol{k}'$. The $z$ component of the scattering vector is given by energy conservation and (5):

$$\begin{aligned}
q_z(q_x, q_y) &= \sqrt{k^2(\mathcal{E}_n - \mathcal{E}_{n'}) - q_x^2 - q_y^2} - K \\
&\approx -\frac{\sigma}{2\pi e}(\mathcal{E}_n - \mathcal{E}_{n'}) - \frac{1}{2k(\mathcal{E}_n - \mathcal{E}_{n'})}\left[q_x^2 + q_y^2\right].
\end{aligned} \tag{D1}$$

Since the full wave function has to be continuous, the scattering matrix elements $S_{nn'}(q_x, q_y)$ can be calculated from the partial wave fronts $\varphi_n(\boldsymbol{r})$ of the paraxial wave ansatz. With initial conditions in a plane $z_{\mathrm{i}}$ before the specimen

$$\varphi_n(z_{\mathrm{i}}) = \delta_{nn'}$$

and after propagation by means of (22) to a plane $z_{\mathrm{f}}$, the scattering matrix are given by

$$\begin{aligned}
&S_{nn'}(q_x, q_y) \\
&\quad = \exp\left[i\frac{\pi}{k(E_n - E_{n'})}\left(q_x^2 + q_y^2\right)z_{\mathrm{f}}\right]\mathcal{F}[\varphi_n(z_{\mathrm{f}})](q_x, q_y).
\end{aligned} \tag{D2}$$

In other words, the coefficients $S_{nn'}(q_x, q_y)$ can be obtained from $\varphi_n(\boldsymbol{r})$ by Fresnel propagation from the plane $z_{\mathrm{f}}$ to the plane $z = 0$, and a Fourier transform

$$\begin{aligned}
&\mathcal{F}[\varphi_n(z_{\mathrm{f}})](q_x, q_y) \\
&\quad = \int_{-\infty}^{+\infty} dx \int_{-\infty}^{+\infty} dy\, \varphi_n(x, y, z_{\mathrm{f}}) \exp[-i2\pi(q_x x + q_y y)].
\end{aligned}$$


[1] S. J. Pennycook and L. Boatner, Nature (London) **336**, 565 (1988).
[2] P. D. Nellist and S. J. Pennycook, Adv. Imag. Elect. Phys. **113**, 147 (2000).
[3] A. Rother, T. Gemming, and H. Lichte, Ultramicroscopy **109**, 139 (2009).
[4] J. Verbeeck, G. Bertoni, and H. Lichte, Ultramicroscopy **111**, 887 (2011).
[5] T. Niermann and M. Lehmann, J. Phys. D **49**, 194002 (2016).
[6] B. E. Warren, Acta Crystallogr. **6**, 803 (1953).
[7] R. W. James, *The Optical Principles of the Diffraction of X-rays* (G. Bell and Sons, London, 1962).
[8] B. E. Warren, *X-ray Diffraction* (Dover, New York, 1990).
[9] B. Borie, Acta Crystallogr. **14**, 566 (1961).
[10] J. Gønnes, Acta Crystallogr. **20**, 240 (1966).
[11] P. Rez, C. J. Humphreys, and M. J. Whelan, Philos. Mag. **35**, 81 (1977).
[12] M. J. Whelan, J. Appl. Phys. **36**, 2103 (1965).
[13] C. R. Hall and P. B. Hirsch, Proc. R. Soc. London, A **286**, 158 (1965).
[14] H. Yoshioka, J. Phys. Soc. Jpn. **12**, 618 (1957).
[15] A. V. Martin, S. D. Findlay, and L. J. Allen, Phys. Rev. B **80**, 024308 (2009).
[16] O. L. Krivanek, T. C. Lovejoy, N. Dellby, T. Aoki, R. W. Carpenter, P. Rez, E. Soignard, J. Zhu, P. E. Batson, M. J. Lagos, R. F. Egerton, and P. A. Crozier, Nature (London) **514**, 209 (2014).
[17] F. S. Hage, D. M. Kepaptsoglou, Q. M. Ramasse, and L. J. Allen, Phys. Rev. Lett. **122**, 016103 (2019).
[18] S. Takagi, J. Phys. Soc. Jpn. **13**, 278 (1958).
[19] C. Dwyer, Phys. Rev. B **89**, 054103 (2014).
[20] B. D. Forbes and L. J. Allen, Phys. Rev. B **94**, 014110 (2016).
[21] E. J. Kirkland, *Advanced Computing in Electron Microscopy*, 2nd ed. (Springer, Berlin, 2010).
[22] I. Lobato and D. Van Dyck, Ultramicroscopy **156**, 9 (2015).
[23] B. D. Forbes, A. V. Martin, S. D. Findlay, A. J. D'Alfonso, and L. J. Allen, Phys. Rev. B **82**, 104103 (2010).
[24] D. A. Muller, B. Edwards, E. J. Kirkland, and J. Silcox, Ultramicroscopy **86**, 371 (2001).
[25] F. F. Krause, D. Bredemeier, M. Schowalter, T. Mehrtens, T. Grieb, and A. Rosenauer, Ultramicroscopy **189**, 124 (2018).
[26] R. F. Loane, P. Xu, and J. Silcox, Acta Crystallogr. A **47**, 267 (1991).
[27] Z. L. Wang, Acta Crystallogr. A **45**, 636 (1989).
[28] C. Fanidis, D. Van Dyck, and J. Van Landuyt, Ultramicroscopy **41**, 55 (1992).

[29] C. Fanidis, D. Van Dyck, and J. Van Landuyt, Ultramicroscopy **48**, 133 (1993).
[30] C. Dinges, A. Berger, and H. Rose, Ultramicroscopy **60**, 49 (1995).
[31] D. Van Dyck, Ultramicroscopy **109**, 677 (2009).
[32] Z. L. Wang, Acta Crystallogr. A **54**, 460 (1998).
[33] C. Cohen-Tannoudji, B. Diu, and F. Laloë, *Quantum Mechanics* (Wiley-Interscience, New York, 1977), Vols. 1 and 2.
[34] N. R. Lugg, B. D. Forbes, S. D. Findlay, and L. J. Allen, Phys. Rev. B **91**, 144108 (2015).
[35] C. J. Joachain, *Quantum Collision Theory* (North-Holland, Amsterdam, 1975).
[36] H. Müller and H. Rose, in *High-Resolution Imaging and Spectrometry of Materials*, Springer Series in Material Science Vol. 50, edited by F. Ernst and M. Rühle (Springer, Berlin, 2003), pp. 9–68.
[37] L.-M. Peng, G. Ren, S. L. Dudarev, and M. J. Whelan, Acta Crystallogr. A **52**, 257 (1996).
[38] C. Dwyer, T. Aoki, P. Rez, S. L. Y. Chang, T. C. Lovejoy, and O. L. Krivanek, Phys. Rev. Lett. **117**, 256101 (2016).
[39] P. Schattschneider, *Fundamentals of Inelastic Electron Scattering* (Springer, Berlin, 1986).
[40] H. Bethe, Z. Phys. **76**, 293 (1932).
[41] K. Huang and N. F. Mott, Proc. R. Soc. London, Ser. A **190**, 102 (1947).
[42] N. Ashcroft and D. N. Mermin, *Solid State Physics*, edited by N. Ashcroft and D. N. Mermin (Saunders College Publishing, New York, 1976).
[43] R. J. Glauber, Phys. Rev. **84**, 395 (1951).
[44] P. Rez, Acta Crystallogr. A **34**, 48 (1978).
[45] J. J. Earney, Philos. Mag. **23**, 577 (1971).